

Long Spin Relaxation Times in CVD-Grown Nanodiamonds

Jeroen Prooth, Michael Petrov, Alevtina Shmakova, Michal Gulka, Petr Cigler, Jan D'Haen, Hans-Gerd Boyen, and Milos Nesladek*

Currently, the primary applications of fluorescent nanodiamonds (FNDs) are in the area of biosensing, by using photoluminescence or spin properties of color centres, mainly represented by the nitrogen vacancy (NV) point defect. The sensitivity of NV-FNDs to external fields is, however, limited by crystallographic defects, which influence their key quantum state characteristics - the spin longitudinal (T_1) and spin transversal (T_2) relaxation and coherence times, respectively. This paper reports on utilizing an advanced FND growth technique consisting of heterogeneous nucleation on pre-engineered sites to create FNDs averaging around 60 nm in size, with mean longitudinal coherence times of 800 μ s and a maximum over 1.8 ms, close to bulk theoretical values. This is a major, nearly ten-fold improvement over commercially available nanodiamonds for the same size range of 50 to 150 nm. Heavy-N doped nanodiamond shells, important for sensing events in nm proximity to the diamond surface, are fabricated and discussed in terms of re-nucleation and twinning on {111} crystal facets. The scalability issues are discussed in order to enable the production of FND volumes matching the needs of sensing applications.

1. Introduction

Nanodiamond (ND) is a fascinating class of nano-material because of its unique properties, such as low cytotoxicity and biocompatibility.^[1–3] NDs can be used for nanoscale sensing based on fluorescent properties of incorporated point (color) defect centres. For these purposes, this type of nanodiamond is referred to as Fluorescent Nanodiamond (FND). Further on, the paramagnetic, e.g., spin properties of color centres, enable using FNDs for sensing the magnetic field noise close to the ND surface, leading to novel measuring concepts such as nano-NMR.^[4–8] Most of the FNDs sensors are based on the nitrogen-vacancy (NV) centre, that has attracted significant attention due to its bright photoluminescence and negligible photobleaching.^[9] The NV centre consists of a nitrogen atom next to a vacancy and has been studied fundamentally and used in initial applications.

The NV spin ground triplet state can easily be manipulated by microwaves at ambient conditions. The crucial challenge for developing nanoscale sensing probes, based on the NV color centres, is to engineer FNDs with high spin relaxation (T_1) and spin coherence (T_2) times, which differ significantly for various types of FNDs, and which limit a wide spread use of FNDs sensors in biology and chemistry fields, for example in drug delivery, bio-imaging, and bio-nanosensors for applications operating at room temperatures. Currently, commercial FNDs have T_1 times in the range of 100 microseconds, while the bulk diamond T_1 limit is about three milliseconds, thus limiting FND use significantly.^[10] Here, we present data on about eight-fold improvement of the T_1 time by Chemical Vapor Deposition (CVD) technique, supported by understanding the underlying physics.


Currently, commercial FNDs are mainly prepared from high pressure, high temperature (HPHT) diamond by milling^[11] and subsequent irradiation and annealing. HPHT FNDs have a typical NV T_1 relaxation time between 50 and 100 μ s.^[12] As the sensitivity of NV center to magnetic fields is limited by the T_1 relaxation time, the ability to engineer FNDs with higher T_1 times would improve the detection sensitivity.^[13] Nevertheless, this requires precise control over particle properties such as size, morphology, defects, and dopants. The HPHT FND approach, based on milling and grinding N-containing bulk diamond, produces FNDs that range in size from around 10 nm to 1 μ m. This mechanical process makes these FNDs highly irregular and jagged, generating a significant amount of spin-active surface

J. Prooth, M. Petrov, A. Shmakova, J. D'Haen, H.-G. Boyen, M. Nesladek
Institute for Materials Research (IMO)
Hasselt University
Wetenschapspark 1, Diepenbeek B-3590, Belgium
E-mail: milos.nesladek@uhasselt.be

J. Prooth, M. Nesladek
IMOMECE
imec
Kapeldreef 75, Heverlee B-3001, Belgium

M. Gulka, P. Cigler
Institute of Organic Chemistry and Biochemistry of the CAS
Flemingovo nam. 2, Prague 166 10, Czech Republic

M. Nesladek
FMBI
Czech Technical University
Sitna 3 105, Kladno Czech Republic

 The ORCID identification number(s) for the author(s) of this article can be found under <https://doi.org/10.1002/qute.202300004>

© 2023 The Authors. Advanced Quantum Technologies published by Wiley-VCH GmbH. This is an open access article under the terms of the Creative Commons Attribution-NonCommercial-NoDerivs License, which permits use and distribution in any medium, provided the original work is properly cited, the use is non-commercial and no modifications or adaptations are made.

DOI: 10.1002/qute.202300004

defects, dangling bonds, and subsurface damage.^[14] Further processing using high energy particle irradiation, employed to create nitrogen-vacancies, can cause internal lattice damage and introduce spin active defects, strain fields, or vacancy clusters. For HPHT nanodiamonds, one usually irradiates them with electrons (e^-), protons (p^+), or He^{2+} and Li^+ ions. An annealing step allows the vacancies to diffuse towards the substitutional nitrogen and create NV centers, while at the same time some of the damage can be repaired. Nevertheless, a study done on several HPHT nanodiamonds irradiated by these methods showed that particles with sizes around 50 to 150 nm had T_1 times between 50 and 100 μ s for those irradiated with e^- , and He^{2+} and up to 150 μ s for particles irradiated with p^+ .^[15] Other studies have shown similar results, with T_1 times ranging around 100 μ s.^[12] FNDs with a size of around 15 nm showed lower T_1 times around 25 μ s.^[10] Another method for large-scale production of fluorescent nanodiamonds (FND) using neutron irradiation is capable of producing significant amounts of nanodiamonds, typically on the order of around 100 grams.^[16] However, the FNDs' obtained T_1 times are short compared to their expected bulk values. In another work, the milling technique has been improved, leading to 1.2 ms T_1 times, however, only a few percent of FNDs contained NV centers.^[17] Chemical vapor deposition (CVD) using isotopically pure ^{12}C as a source gas was used to grow diamond films, which were then again milled to produce FNDs.^[18] Using this technique T_2 coherence close to 400 microseconds was reported. However, all methods employing milling face challenges related to defect formation, chipping, and the production of irregular sizes caused by the milling process. One of the techniques to eliminate milling is based on the etching of diamond to form diamond nano-pillars through the use of nano-processing and nanolithography.^[19] This approach results in enhanced diamond T_2 spin coherence times of approximately 210 microseconds. However, it should be noted that this technique produces nanopillars rather than round nanodiamonds, which may not be suitable for certain applications such as cellular biology, where nano-pillars may pose risks of piercing the cell membrane.

A FND preparation technique, pursued here, is the direct nanocrystal growth using CVD. This means that instead of growing microcrystals and milling them down to nanoparticles in a top-down approach, we grow them directly on the substrate in a bottom-up way, avoiding surface defects and shape irregularities, which are introduced through the milling process. To initiate the growth of nanodiamonds, a seed with a diamond structure is required,^[20,21] such as detonation nanodiamond (DND). However, this technique would quickly result in the formation of a thin film. In particular, for achieving high T_1 times it is necessary that the crystals grow individually and develop clear facets. In that sense, the nanocrystalline nature would reduce the T_1 times. Alternatively, diamondoids can initiate nucleation; for example, pentamantane can be used for seeding.^[21–23] This requires bonding of diamondoids to the substrate, because diamondoids easily sublimate at temperatures lower than the diamond growth temperature,^[24] limiting diamond nucleation. In all these cases, mainly, a continuous nanodiamond film is formed. In this paper, we adopt a different approach, one that is both simple and easy to perform i.e., heterogeneous nucleation. Spontaneous heterogeneous nucleation, meaning nucleation on substrates chemically or crystallographically different from the material to be grown, has been employed before, but the resulting nucleation densities

are extremely low.^[21] Therefore, to enhance it, one can perform a pre-treatment such as mechanical nano-roughening.^[25] The advantage of these methods is that no seed is required, and one has, in theory, complete control over particle properties from the start of the growth.

This technique of synthesizing nanodiamonds through heterogeneous nucleation results in increased T_1 times of around 800 μ s for particles averaging 60 nm, which is an eight-fold improvement compared to HPHT FNDs, where T_1 reaches roughly 100 μ s for similar-sized particles. The maximum T_1 times exceed 1.8 ms, which is close to bulk diamond values. For this study, we have performed measurements over several growth conditions, and the T_1 is consistent between samples.

Since the NVs are naturally generated during the CVD process, consequently, the potential deterioration of NV spin coherence properties is limited, compared to when implantation is used. However T_2 times will be influenced by the spin bath induced by paramagnetic defects generated during growth, or by surface defects.^[4,18,26] In the CVD process, the NV yield is rather low, and a large portion of N forms paramagnetic substitutional defects. Therefore, in this work, we also evaluate NV formation efficiency.

Further on, we address the following questions related to achieving the highest T_1 times: We study FND growth at different conditions, such as the substrate temperature, and we investigate the T_1 value's dependence on the nanodiamond size. Due to the interest in biological applications and the need to have the NV center in nm depth from the FND surface for increased sensitivity to the environment, we have developed an N_2 -pulse doping technique that allows us to increase the N_2 concentration in the gas phase at the very end of diamond growth, producing highly nitrogen-doped FND shells. We studied T_1 in such samples and compared them with FND samples without the shell. We find that re-nucleation and twinning are present due to high N-concentration in the gas phase, and defects generated in this step can still limit achieving higher T_1 times.

2. Results and Discussion

2.1. Nanodiamond Growth

To nucleate diamond nanoparticles with high density, we perform nano-roughening followed by an optimized and specifically designed CVD process, **Figure 1**. We grow two sets of samples: reference particles (low-doped), which have no additional nitrogen added, and shell-doped particles, which have a nitrogen pulse applied at the final step of their growth. To grow well-separated individual nanocrystals rather than films, we have optimized our pretreatment method, allowing us to tune the ND coverage on the substrate by modifying the roughening duration. With this process, we can produce well-faceted nanodiamond crystals, **Figure 2**. In the Supporting Information, one can find an additional set of SEM images, showing ND crystals of small sizes, however taking sharp images on non-conductive particles is challenging. On some samples, a Pd-Au layer was deposited to enhance the imaging process.

Adjusting the duration of the ultrasonic treatment allows us to tune the nucleation density and produce individual crystals at a higher density. Assuming a roughly 30% coverage, a particle diameter of 50 nm, a growth rate of 1 micrometer per hour, and a 15 cm substrate, it is possible to obtain about 2.6 mg of NDs

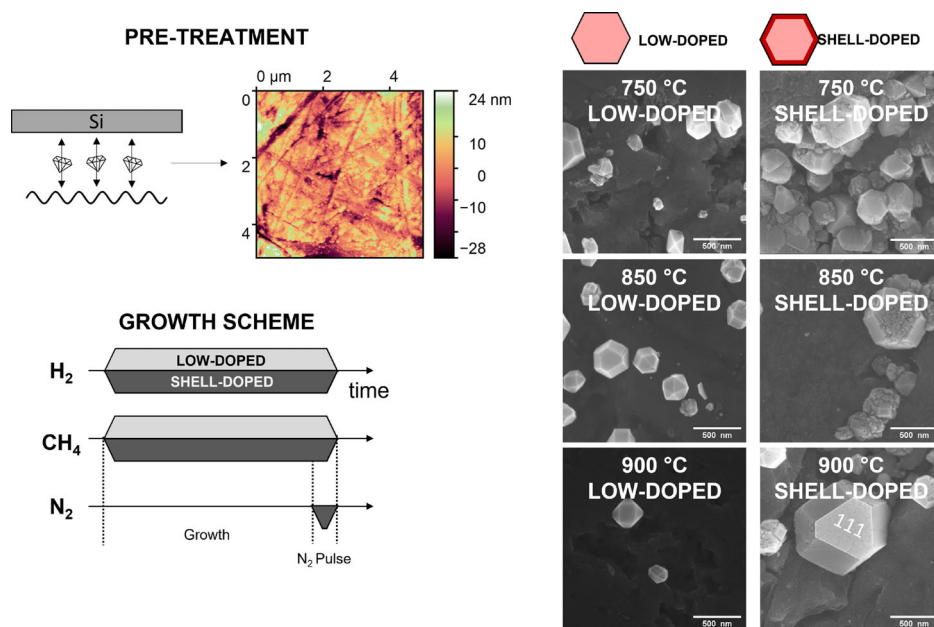


Figure 1. A nano-roughening pre-treatment on silicon is performed by using an ultrasonic vibration table on which diamond micro-particles are spread and on which the substrate is vibrated. This produces nano-roughness, and leaves carbon traces on the substrate surface, pictured in the AFM image. The growth scheme shows the introduction of gasses during the growth stage. As a base diamond material, we use low N-doped samples, whereas for the shell-doped particles, we created in addition a highly nitrogen-doped shell. Images of particles grown at 750, 850, and 900 °C taken with a GeminiSEM 450 at 5 kV. Left side shows low-doped samples, with nitrogen shell-doped samples on the right. Shell-doped particles show preferential re-nucleation on their {111} facets due to the too-high nitrogen concentration, whereas low-doped particles show no such structures. Twinning can be found for all conditions.

using such a system. As illustrated in **Figure 3**, at a temperature of 700 °C, roughly 35% of NDs fall within the range of 30–60 nm, which would allow us to get roughly 1 mg of these particles within a single run, enough for further chemical processing.

In this work, we do not concentrate on achieving high quantities and grow on small, 5 x 5 mm² silicon substrates. Removal of NDs from the wafer can be done through etching, however this process requires the use of HF acid, which is undesirable. Another approach is to use a thin metallic intermediate layer,^[27] on which NDs can be grown. The wet etching of such a layer is instantaneous as it can be very thin, 50 nm or less, making the process efficient. Using intermediate layers, NDs can be deposited on various substrates such as quartz, sapphire, and others, allowing for reusability. We perform preliminary measurements on NDs grown on an intermediate molybdenum layer (see Supporting Information) to demonstrate the feasibility of the proposed methods, however most of the work is done on particles grown on silicon substrates. We have measured T_1 of nanodiamonds grown on molybdenum inter-layers and achieved similar T_1 as those on silicon, see Supporting Information.

2.2. Size and T_1 Distributions

Using a combination of scanning electron microscopy (SEM) and photoluminescence mapping (PL), we are able to determine the size of our particles and the average amount of NVs they contain and therefore find important correlations, such as the product of the N incorporation rate and the NV generation yield, as discussed further. We match PL distributions to size distributions

obtained with SEM using the shape of the curves. With this, we find the correspondence between size and photoluminescence for a given laser power. This correspondence is further used to determine sizes of specifically those particles that we measure T_1 for.

For this evaluation, we use both low-doped FNDs and FNDs equipped with a 10 nm thick highly N-doped shell, as discussed in the Experimental Section. The size distributions of the nanodiamonds grown at various temperatures were first determined using SEM. Further on, by identifying the FNDs in the PL map and knowing the PL rate per NV, we correlate the size of particles to their T_1 time. The SEM photos are analyzed with ImageJ and Python, while the PL images are analyzed with a custom-made Python program that uses the SciPy package. Due to thresholding and blurring, we estimate our inaccuracy on the diameter to be around 15 nm, or two pixels, given by the used SEM magnification. This error results from either overestimating or underestimating the border of our nanodiamonds. The Experimental Section and Supporting Information provide a detailed description of the complete workflow.

Figure 3a, for the NV shell doped samples, and Figure 3b, for the low-doped samples, both display the FND size distributions. The computed size distributions from PL are shown in blue, and SEM distributions are shown in red. The diameter was determined from the PL intensity using the formula below; for the derivation, see the Supporting Information:

$$d = \sqrt[3]{\frac{3I_{\text{tot}}a^3}{4\pi \frac{[N_2]}{[CH_4]} I_s N_i N_c}} \quad (1)$$

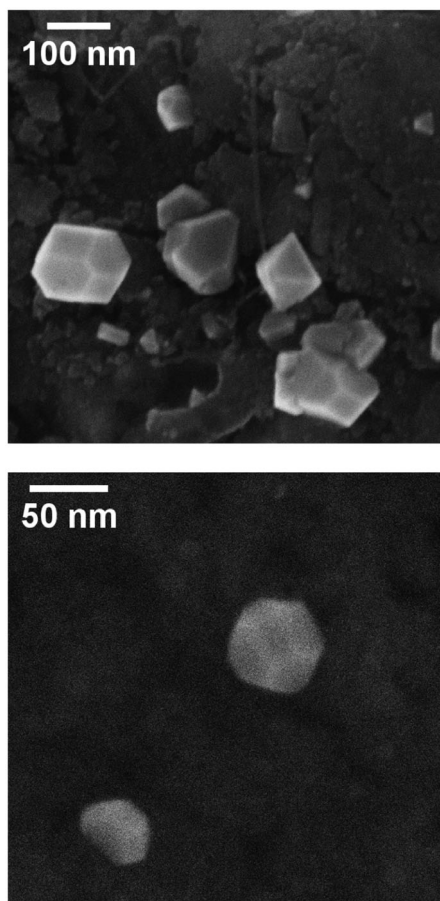


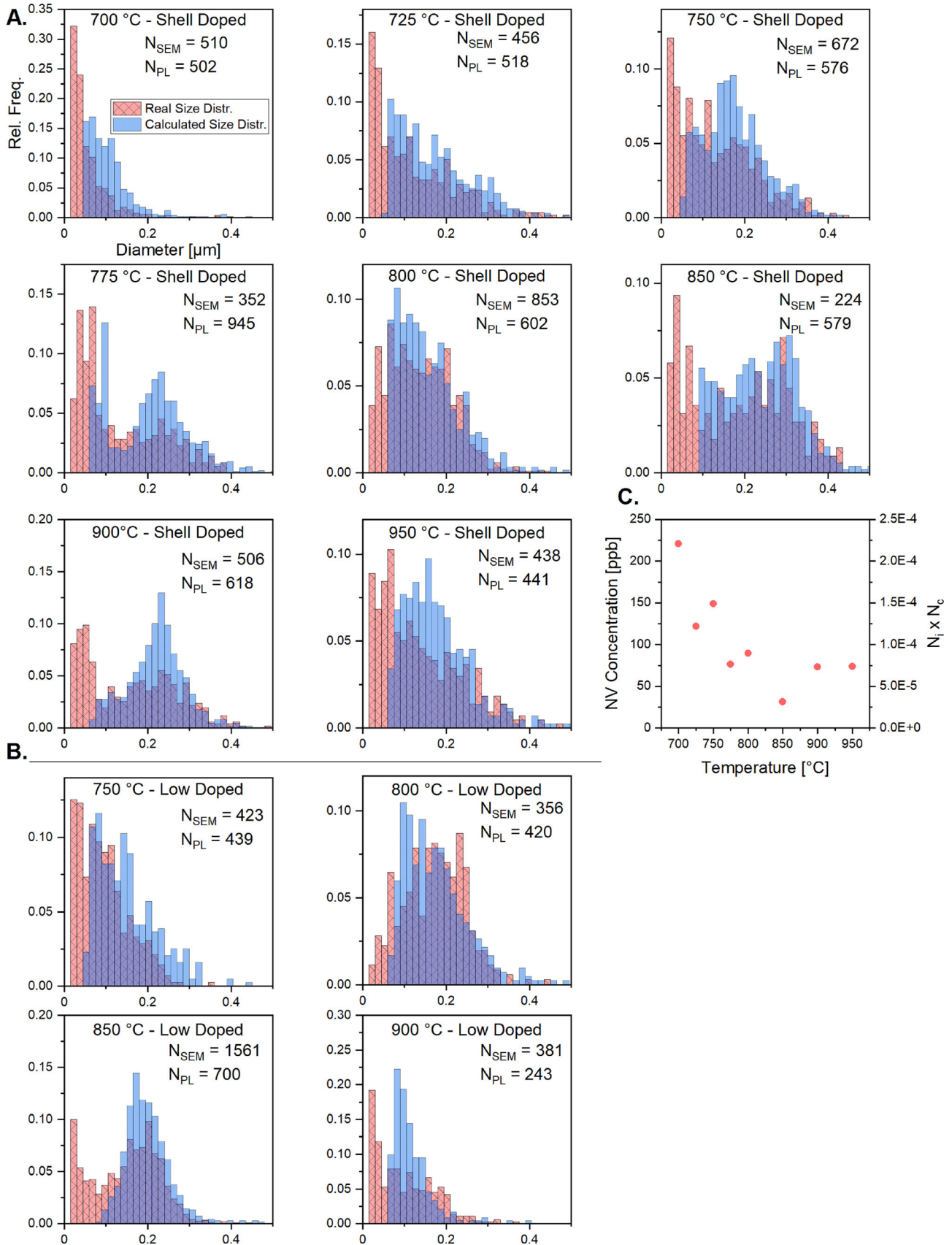
Figure 2. SEM images showing typical particle morphology for our growth conditions. Particles shown here do not have a δ -doped shell. Additional images can be found in the Supporting Information.

with d being the diameter, I_{tot} the total measured photoluminescence of a single diamond particle, a the diamond unit cell size equal to 3.58 Å, $[N_2]/[CH_4]$ the nitrogen to methane ratio, I_s the single NV photoluminescence under constant laser power, N_i the nitrogen incorporation rate, and N_c the N to NV conversion rate. The FNDs grown at 700 °C exhibit the narrowest size distribution in Figure 3a, with a mean of about 58 nm. The mean size increases to higher values as the temperature is raised, and in some conditions, a secondary peak can be seen for larger particle sizes. During our image analysis, we employ a technique known as “water-shedding”, which is a powerful image analysis technique for segmenting coupled particles and detecting their boundaries.^[28] As a result, this peak cannot be attributed to several clustered FNDs mistaken for one particle. In addition, SEM images visually display a collection of smaller particles, see the Supporting Information. Due to the nature of sample pretreatment (see the Experimental Section) we anticipate that some of the diamond debris from the roughening is still left on the silicon substrate, even after the cleaning step, and behaves as seeds. We expect that the size of this debris exceeds the critical nucleation size, allowing it to continue growing throughout the CVD process and causing a distribution of larger sizes (2nd peak in the distribution). We attribute the peak on the left, for

FND of 50–60 nm in size, to heterogeneous nucleation, i.e., sp³ carbon residua, which transform to nuclei after an incubation period.^[29] Pre-nuclei compete to grow or are etched until they eventually surpass the critical nucleation size, at which point they can continue to expand. We surmise that the occasional lack in the peak division between primary and secondary ones is due to the cleaning process’ reproducibility following nano-roughening, i.e., removal of nanodiamond debris. Table S2 (Supporting Information) provides a detailed description of the size distributions’ mean, 75th, and 99th percentiles, meaning 75 % and 99 % of particles are below those thresholds, respectively.

Equation 1 is used to fit the PL distribution, shown in Figure 3a,b, to the SEM distribution. To match the PL conditions used for T_1 measurements, measurements were performed at 50 μ W of laser power. For these small laser powers, the PL distribution onset (blue) starts at a larger FND size with respect to the SEM detected distribution onset (red), Figure 3. This is due to the low PL luminescence counts related to small FNDs. We could also access the first peak in the distribution spectra by using higher laser powers, confirming that both the PL and SEM analyses are well matched (see the Supporting Information for more details). The same $[N_2]/[CH_4]$ and I_s are used for shell-doped samples grown at various temperatures. As the $N_i \times N_c$ product is the only unknown variable in Equation 1, it becomes the fitting parameter for the PL distribution. We find the value of the product $N_i \times N_c$ for different temperatures by matching the PL distribution (Figure 3a-b-blue), to the SEM distribution (Figure 3a,b-red). This approach allows us to determine the NV concentration at different temperatures, Figure 3c. We show that NV formation increases six times at 700 °C compared to 850 °C. A similar result was obtained previously by Tallaire et al.,^[30] where the NV concentration for bulk growth at 780 °C increased by three times compared to 880 °C. However, in their experiment, the growth was performed exclusively on the {100} facet, and here, interestingly, we have a mixture of both {100} and {111} facets. Since nitrogen incorporation is more efficient in the {111} facet,^[31] we expect that it is the N-incorporation in the {111} facets that determines the final N-content in the case of our nanodiamond growth as compared to [30]. We also note that the fitting values, used in Figure 3, obtained for the FNDs with a nitrogen shell-doped layer, which we discuss in detail below, were very similar to the corresponding (i.e., same temperature) low-doped samples, i.e similar $N_i \times N_c$ for similar temperatures). The fact that the δ -doped shell only has a small influence on the total luminescence is discussed later in the text. As seen in Figure 3b, the distributions for both cases match well, thereby also supporting our theoretical model for size distribution calculation. Figure S15 (Supporting Information) also shows the calculated diameter of a particle compared to its measured SEM size, having only a small error of a calculated size of roughly 280 nm to a measured size of 306 nm.

Figure 4 shows all T_1 measurements executed on the shell-doped nanodiamonds grown at different temperatures using a 50 μ W laser. T_1 time ranges between 100 and 1800 μ s. This spread could be a consequence of varying morphology between NDs, Figure 1, which depends on how a particle evolves from its nucleation to its final crystal shape, in particular, depending on if {100} or {111} facets are more prominent, defects can be different. We achieve T_1 times on average of about 800 μ s - a major improvement over HPHT nanodiamonds, which achieve T_1 times up 150



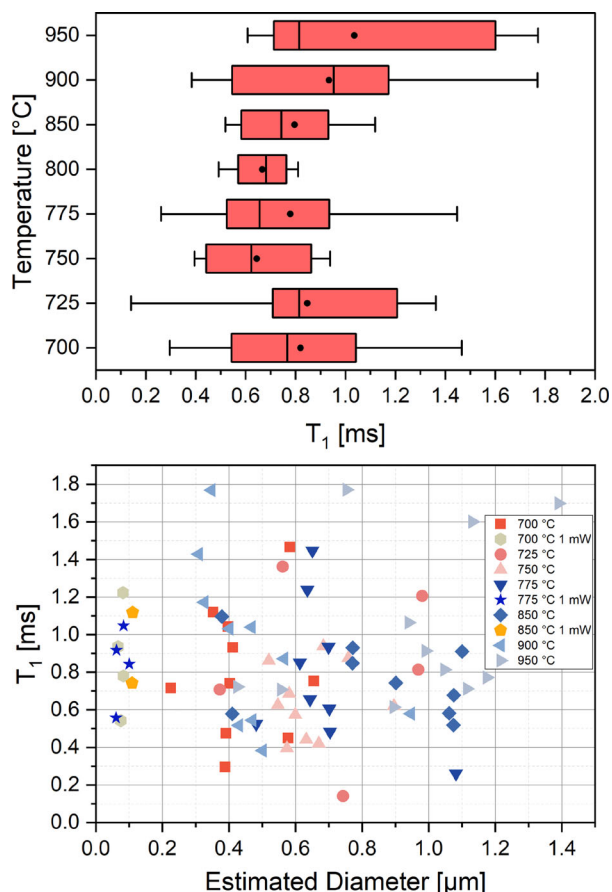


Figure 4. Top: Overview of the range of measured T_1 times for all shell-doped samples, obtained with subtraction of a purely optical measurement with a microwave measurement. Mean relaxation times stay relatively consistent, Table S2 (Supporting Information). Bottom: Calculated particle size from its luminescence for each measured T_1 time. Unless specified, measurements were done at 50 μ W. Two samples were measured at 1 mW as at lower power small particles blend into the background luminescence, see the Supporting Information. For measurements at 1 mW, specifically low-luminescent particles were chosen. While average T_1 is consistent between different samples, within the sample particles with strongly varying T_1 times can be found. This is most likely due to varying crystal morphology throughout the sample.

μ s in particles of roughly 50 – 150 nm.^[15] T_2 times do not show such improvement (see the Supporting Information), this we attribute to be due to the paramagnetic defect density, such as P1 centers providing the spin bath. Indeed, according to the growth conditions, we expect the concentration of nitrogen to be around 10 ppm, while NV density is in the range of 100 ppb, whose ratio is significantly higher than for implanted and annealed HPHT diamond and is the limiting factor for T_2 .^[32] We also show that in our samples, T_1 times seem relatively independent when increasing the mean particle size (Table S2, Supporting Information).

Figure 3. A. Overview of the size distributions by SEM (red) and by calculation from PL distribution (blue) for shell-doped samples. B. Similarly calculated distributions for low-doped samples. The calculations for corresponding temperatures used the same reactor impurity, single NV count and $N_i \times N_c$ rate. C. NV concentration and the product of nitrogen incorporation N_i and conversion rate N_c as a function of temperature showing a 6.25 fold increase at 700 °C as compared to 850 °C. N_{SEM} and N_{PL} are the number of particles measured for the SEM and PL distributions, respectively. Particles smaller than 70 nm are absent in the PL distribution, since the sample images used for the distribution analysis are obtained at low laser power.

NDs smaller than 200 nm have to be measured with a higher laser power of 1 mW due to their weak luminescence.

2.3. Effects of Nitrogen Doping

In this paragraph, we compare the morphology of low-doped and shell-doped FNDs. A high nitrogen pulse is performed to engineer an outer, NV-doped shell, comparable to δ -doping in bulk diamond. This technique is described in the Supporting Information. The effects of the high nitrogen doping on the FND morphology are studied using SEM and compared to the first set of FND samples grown under low N-doping conditions. Figure 1 shows the difference in the surface morphology for low-doped as compared to shell-doped FNDs, grown at similar temperatures. The growth conditions for low doping were selected to lead to a mixture of {111} and {100} facets and cuboctahedron shapes at about 850 °C with an alpha parameter of roughly 1.75.^[33] Whilst low N-doping leads to clean facets and nearly perfect crystal morphology, high N-doping across all growth temperatures causes major twinning. The thin diamond layer grown under the nitrogen pulse at the final step of the growth cycle shows re-nucleation and multi-twinning growth on the {111} facets, while the {100} facets remain clean without re-nucleation. The effect of twinning in {111} facets is known, especially for high N_2 gas addition.^[34] Due to this multi-twinning and re-nucleation, the high N-doped shell is highly defective, and we observe a decrease in relaxation time T_1 as compared to low-doped growth only, displayed in Figure 5. We could show that the growth at high nitrogen doping conditions leads to generation of surface defects, of which the integrated magnetic field reduces the T_1 time.^[8] Also, the crystallographic defects enable other recombination channels and consequently the PL from the shell-doped layer is reduced. Another characteristic is that the T_1 measurements discussed in the next section are more difficult to execute due to the baseline drift. In particular, for example, by applying a MW π -pulse, the PL trace does not show the population inversion, as expected, shown in Figure 6. However, by using the procedure (described in the following section), we can correct for the time-dependent baseline. The decrease in relaxation time is very likely to be therefore an effect induced by the increase in surface area due to multi-twinning and due to an enhancement of surface spins density.^[34] As mentioned in the previous section, in Figure 3 we have used the same fitting parameters to calculate the size distributions for the low-doped crystal growth as for the shell-doped size distributions. This makes us believe that the NV formation during the high nitrogen pulse, relative to the N concentration in the gas phase, is low and most of the nitrogen is incorporated as N_s .

2.4. Microwave T_1 Measurements

Nanodiamonds are vulnerable to NV charge state alternations.^[35] If charge state alterations are dynamic, they will introduce a

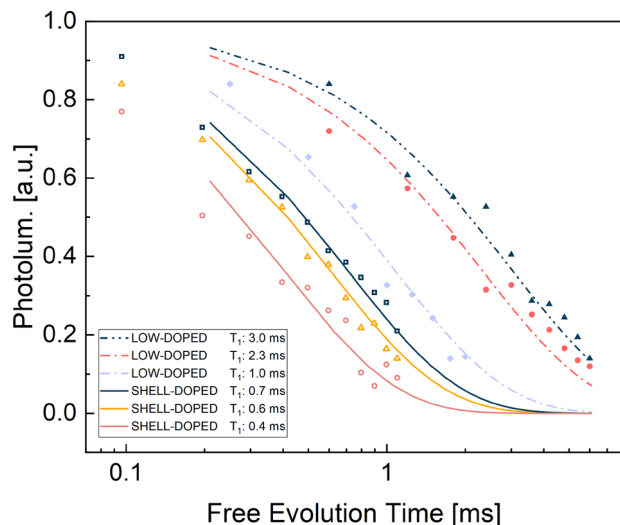


Figure 5. Experimental data fits for shell-doped and low-doped nanodiamonds. Addition of a nitrogen pulse (shell-doping) to the growth sequence decreases the relaxation time from $T_1 \in [1\text{ms}, 1.7\text{ms}]$ to $T_1 \in [0.5\text{ms}, 0.9\text{ms}]$. Particles were calculated to be around 500 nm. Shell-doped nanodiamonds show lower T_1 times than the FNDs grown without shell-doping.

baseline drift to the measurements, because the free evolution would, additionally to the spin state, also involve reaching charge state equilibrium. These alternations can occur via photoionization of N, NV, and other defects present in FNDs, but also by redistributing the charge on the ND surface. This is quite natural, taking into account the possible band bending effects and their influence by surface termination.^[36] As the band bending can range over several nm or more,^[37] the charge alterations are naturally present. Band bending can occur for example due to adsorbates present at the surface.^[38] Here, we have measured on the naturally grown nanodiamonds without any additional treatment, as we preferred not to detach the FND from the

silicon surface due to their small amounts and to prevent any use of chemicals that might lead to FND pollution by substrate surface etching. Diamond surface adsorbates can also change upon laser illumination, influencing the band bending,^[36] for example, by flattening it by charge carrier generation. Also, PL from other defects can contribute to the detected signal. Therefore, during the measuring of T_1 relaxation time, the resulting PL curve contains both the nitrogen-vacancy relaxation and additional defects relaxation. For these reasons, it is necessary to properly analyze the PL time dependence to distinguish between T_1 relaxation and parasitic effects.

In order to exclude these parasitic effects, we perform measurements by using purely optical T_1 detection and also measurements with π -pulse microwave application.^[14] Microwave radiation swaps the population of spin states zero and one, and this process is followed by a PL readout. If photoluminescence decay were a result of NV spin relaxation only, the relaxation curve would be mirrored after the MW-induced population swaps. Measurements of differences in time traces for purely optical and optical with MW driving have therefore been used^[4] to fully decompose the PL decay spectra into spin flip dependent and independent processes. While for purely optical spin polarization and decay measurements, we anticipate a decaying PL curve to the steady state, when using π -pulse microwave driving in between the laser pulses, we anticipate a rising PL with time.

As stated, our measurements have revealed the presence of an additional non-spin baseline relaxation, most likely originating at the charge alteration processes. Figure 6 shows the results of the three measurement sequences described in the Experimental Section, Figure 9, performed simultaneously. The “No MW” curve indicates the population of $m_s = 0$ spin state after relaxation from $m_s = 0$ state, the “MW After Free Evolution” curve indicates the population of $m_s = 1$ state after relaxation from $m_s = 0$, and the “MW Before Free Evolution” curve indicates the population of $m_s = 0$ after relaxation from $m_s = 1$. Subtraction of the curves that correspond to relaxation from $m_s = 0$ should allow us to correct for the baseline. However, the difference between the

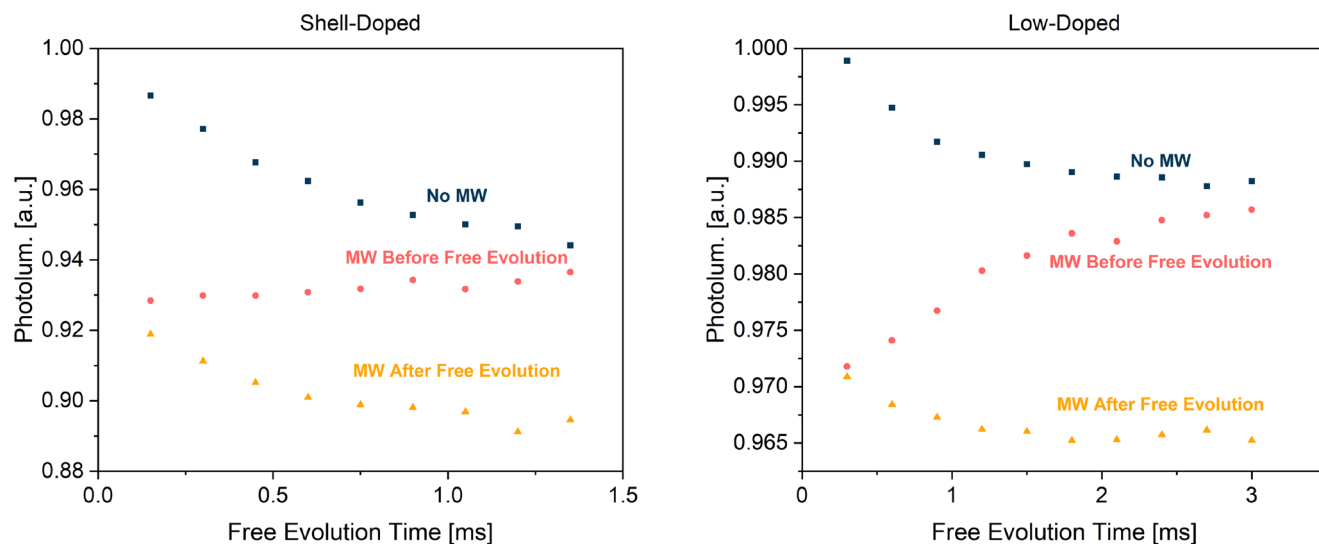


Figure 6. Photoluminescence as a function of free evolution time for shell-doped (left) and low-doped (right) nanodiamonds. Low-doped FNDs show a stronger inversion of the relaxation-related decay.

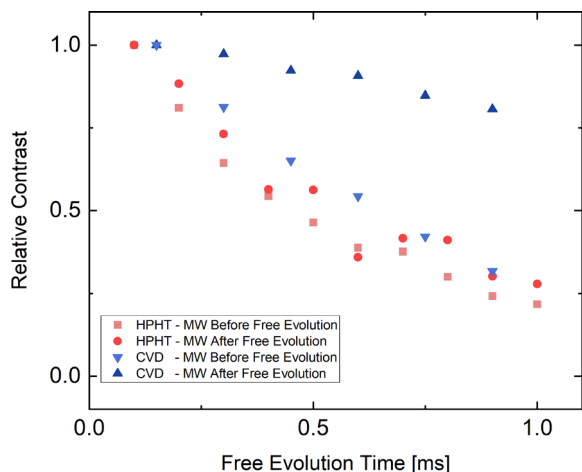


Figure 7. Difference between photoluminescence signal with and without microwave application. Data for the high T_1 sample diverges with respect to microwave pulse position, but data for the reference sample does not. For this comparison particles with similar T_1 are found in both samples.

curves changes very little, as they do not fully converge, causing a large error on the fitting parameters. Therefore, we choose to subtract the curve showing $m_s = 1$ relaxation from the curve showing $m_s = 0$ relaxation. Even though the relaxation path from $m_s = 1$ is different than from $m_s = 0$ state, and the decay from $m_s = 1$ is biexponential, the population of $m_s = 0$ state still changes with the same time constant.^[39] We solve rate equations to show that the T_1 is the same in both cases (see the Supporting Information). The T_1 values presented in Figure 4 are calculated this way. We present a more complex background subtraction procedure in the Supporting Information.

The fact that the two curves for relaxation from $m_s = 0$ do not converge indicates that the state to which the system relaxes on the timescale of the measurement might not be a full statistical mixture of the three triplet states. This is an unexpected result, as thermal energy at room temperature should be higher than the splitting between the triplet states. We confirm that we have no leakage of laser light, as such leakage would indeed result in breaking the symmetry between the triplet states. We measure that AOM attenuation exceeds 50 dB for 10 μ W laser power, which means that initialization time will increase from approximately 3 μ s to more than 300 ms. Considering that the longest free evolution time in our measurements is 3 ms, the effects of laser leakage are negligible. Although the origin of this effect remains unconfirmed, our hypothesis is that it can be connected to, e.g., observed charge switching of NVs under illumination or in the dark,^[40] or possibly to surface Fermi level pinning.^[36] For example, there can be an upward band bending, as we observed, at the surface leading to higher population of NV^0 states.^[36] When the band bending slowly relaxes (the charge redistribution at the surface is known to be slow, often in the range of minutes), the NV^0 will slowly transform to NV^- state in which the $m_s = 0$ population will be augmented^[41], the system will return to an equilibrium statistical mixture between the $m_s = 0$ and ± 1 states, on the moment when the band bending relaxation stops. Notably, we do not observe this anomaly in nanodiamonds prepared with a standard method, i.e., HPHT nanodiamonds, **Figure 7**.

2.5. Referencing

For comparison of T_1 values in HPHT and CVD-FNDs, and also to verify the reliability of the T_1 protocols, a reference measurement is carried out on HPHT NDs with an expected T_1 time of roughly 100 μ s.^[12] **Figure 8a** shows T_1 measurements on four different nanodiamonds, three of which show relaxation times very close to the expected values. The dependence of these relaxation times on laser power is also measured, as shown in **Figure 8b**. Measurements are performed on the same nanodiamond, but with varying laser power. Lower laser power shows a longer T_1 time (140 μ s) compared to higher laser power (76 and 91 μ s). However, it has to be noted that lower laser powers (if only shorter laser pulses are used) are less reliable, as full initialisation is not achieved, as seen in **Figure 8c**. Additionally, the photoluminescence response of an NV center depends on laser power, which is why in **Figure 8c**, the readout of the thermal state (dashed lines) shows different pulse shapes for different laser powers. Although, the population inversion after a MW pulse properly occurs at higher laser power, showing that HPHT has a more stable surface. In that case, we used oxidized HPHT FNDs from [42]. On the other side, this highlights the need for using both the MW and optical T_1 measurements to correct for the FNDs that are not oxidized or in contact with a liquid or other environment.

3. Conclusion

We fabricated fluorescent nanodiamonds with a high T_1 spin relaxation time, exceeding the current limits of HPHT nanodiamonds. To this end, we have performed CVD nanodiamond growth based on heterogeneous nucleation on pre-engineered surfaces. By measuring the FND size distributions and attributing them to their T_1 times, we show that we can achieve high mean T_1 times in particular 800 μ s with a maximum over 1.8 ms for nanoparticle sizes averaging 60 nm at 700 $^{\circ}$ C. This is about eight times higher than commonly found in commercially available HPHT nanodiamonds and already closer to the T_1 bulk diamond values. The regular diamond shapes and low density of defects are probably playing a major role in reaching high T_1 times. We have found out that the T_1 time can easily be incorrectly evaluated from photoluminescence relaxation due to, probably, photoionization of other defects or band bending changes occurring on the surface of NDs when illuminating with laser, as discussed in the Supporting Information. This is particularly relevant if FNDs are exposed to a time-varying environment, such as a biological environment. By measuring the SEM particle size and mapping the PL using developed dedicated software, we could determine the product of the N incorporation from the gas phase and the NV generation yield. The calculated N incorporation rate to FNDs is in the range of 1%, suggesting that the NV incorporation still occurs mainly via {111} facets. Further on, we attempted to fabricate an NV-doped shell around the core ND by pulsing nitrogen at the final step of the growth; however, due to high doping, we created a highly re-nucleated {111} surface, which is defective. Thus, further optimization to avoid the multi-twinning and re-nucleation for N-doped films together with a high incorporation is necessary to prepare smooth facets with high T_1 times with highly dense ensembles. Moreover, our par-

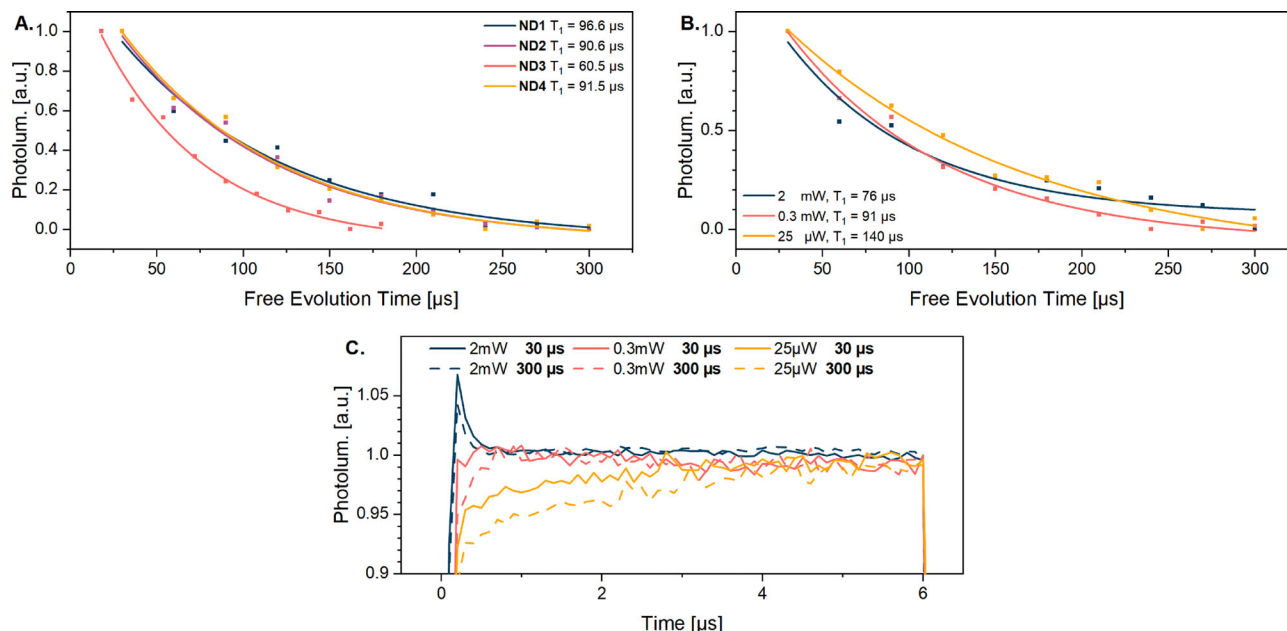


Figure 8. A. Relaxation time measured for different HPHT nanodiamonds similar to those used in [12]. The difference between the nanodiamonds is within error, 100 μs is assumed to be the characteristic relaxation time for these samples. B. Relaxation time was measured for different laser powers. T_1 decreases with increasing laser power. At low powers, NV centre initialisation does not happen or happens to a small extent. C. Time-resolved photo-luminescence during readout pulse of 6 μs , before (solid) and after (dashed) full NV relaxation.

ticles exhibit approximately ten times lower photoluminescence compared to conventional HPHT nanodiamonds. Although previous studies have successfully conducted quantum measurements and tracking using nanodiamonds hosting single NVs within cells,^[43] further improvement in the ND luminosity can be achieved by an additional irradiation treatment, which would increase the NV concentration and reduce partially the N spin bath.

While our nanodiamonds show enhanced relaxation times as compared to HPHT nanodiamonds, there is still further research needed to increase the nanodiamond yield. In order to achieve sufficiently large amount of FNDs for chemical processing, one can use, for example, large area growth systems, such as Linear Antenna MW reactors.^[44] FNDs can be grown on intermediate layers, which are easy to chemically etch away to release FNDs and without the need to dissolve large amounts of the substrate material. We estimate that several milligrams of FNDs can be produced in one CVD deposition run. In addition one can grow on 3D structures such as porous media, nanotube arrays^[45] or similar, to further increase the FNDs amounts deposited in one run.

4. Experimental Section

MW Plasma Reactor: A home-built plasma-enhanced chemical vapor deposition (PE-CVD) diamond reactor (See the Supporting Information), was used to grow nanodiamonds. The growth was controlled with custom-made Python software that communicates with the reactor's Programmable Logic Controller (PLC), which enabled us to had precise control over growth parameters. The MW source consists of a 2.45 GHz microwave generator connected to a waveguide and had a maximum power output of 1.5 kW. Nanodiamonds were grown on Si substrates with sizes of 5 x 5 mm². The gas mixture and growth conditions were discussed below.

Nanodiamond Growth: ND nucleation pre-treatment on all samples was carried out after an initial ultrasonic cleaning using ethanol, followed by subsequent nano-roughening of the substrate with diamond powder using an ultrasonic vibration table (Vibromet Polisher) and 80–120 μm -sized diamond particles (Custodiam 80/120 Mesh) on Si substrates. The samples were again cleaned ultrasonically using ethanol and dried under nitrogen gas flow.

Following their cleaning, the samples were placed within the diamond reactor, which was pumped down to its minimum base pressure of 1.1 E-8 mbar. Two sets of samples were grown: low nitrogen doped and FND with a highly N-doped shell. The substrate temperatures were varied from 700 to 950 °C (see Table S2, Supporting Information for the full list) as measured with a calibrated single wavelength pyrometer. The growth was carried out at a constant 1% methane (4 sccm) addition in hydrogen (396 sccm), a pressure of 120 mbar, and a power of 1.0 kW for 10 min. For the growth of the low doped FND particles, it use H₂ gas with 10 ppm N₂. It also carried out the pulsed N-doping technique, where shell-doped samples had 5 sccm of N₂ added during the final 30 s leading to the growth of a δ -doped shell with an intent to generate NVs close to the surface of the diamond particles. The full details of the pulsing technique could be found in the Supporting Information.

Optical Setup: Figure 9 depicts the quantum confocal setup used for measurements. It consisted of a 532 nm laser beam modulated by an acousto-optical modulator (AOM) for the generation of laser pulses. A dichroic mirror was used to direct green light to the sample and red photoluminescence light from the sample to an avalanche photo-detector (APD) or a CCD spectrometer using a 0.95 N.A. objective. T_1 measurements were performed with a 650 nm long-pass filter, a 700 nm short-pass filter was used for imaging purposes to cut-out the SiV luminescence. The silicon substrate with grown nanodiamonds was glued to a PCB, over which a 50 μm thick wire was soldered. Microwaves could be applied through this wire, which was terminated with a 50 Ohm load.^[46] The setup was run with custom-made LabView software.

High-Resolution SEM: High-resolution SEM imaging was performed with a Zeiss 450 FEGSEM with Gemini two Optics at 5 kV to study their morphology and to see the effect of nitrogen pulsing.

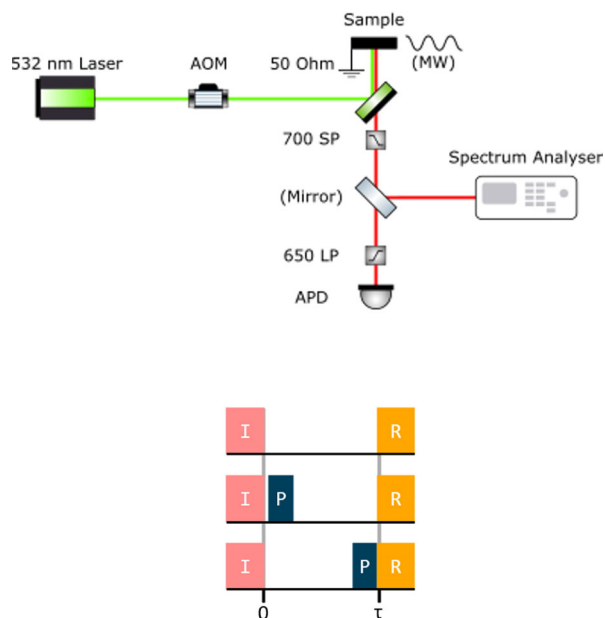


Figure 9. Top: Schematic overview of the measurement setup. Standard confocal setup with the possibility to apply microwaves. Green laser (532 nm) goes through an acousto-optic modulator (AOM) to the sample, illumination from the sample is collected through wavelength filters to an avalanche photodiode (APD) or to a spectrometer. A dichroic mirror is used to combine sample irradiation with light collection. A microwave wire is placed over the sample surface for T_1 pulsed measurements. A 650 nm long pass and 700 nm short pass filters are used. No filter is used for measuring spectra. Bottom: Measurement sequences used for T_1 determination. Each sequence consists of an initialization pulse (I) followed by free evolution time (τ), when no external perturbation is applied, and a readout pulse (R) in the end. The first sequence is a purely optical measurement, the other two sequences have an additional microwave π -pulse (P) right before or directly after free evolution.

Size Distribution Analysis. Size distribution analysis was performed by several image analysis tools, in particular by combining high-contrast SEM images taken by a FEI Quanta and maximum-filtering photoluminescence imaging (see the Supporting Information).

T_1 Measurements: To determine the relaxation times of the grown nanodiamonds, various optical and microwave pulsing schemes, as shown in Figure 9, were compared. A small external magnetic field was applied to split the resonances.

Initialization of the NV centres in the nanodiamonds was achieved using a 532 nm laser pulse. After a time delay (τ), a readout of the color centres was performed. During this delay, NV centres relax to their thermal equilibrium state with time constant T_1 . By varying τ we obtain a full relaxation curve for the specific nanodiamond. Optionally, a microwave pulse was inserted either between the initialization pulse and free evolution or between the free evolution and the readout pulse. The former changes the relaxation path from $ms \pm 1$, while the latter merely swaps the state population before readout.

Due to laser illumination and subsequent photoionization, the charge state of the NV centre could change. As such, both optical and MW assisted T_1 measurements were performed, with further subtraction of the results in order to exclude the charge state alteration effects on the PL decay.^[47] Also, the baseline relaxation was important for some FNDs and it discussed this in detail in the Supporting Information.

Supporting Information

Supporting Information is available from the Wiley Online Library or from the author.

Acknowledgements

J.P. and M.P. contributed equally to this work. The author would like to acknowledge the following projects: Diamond for chip-based quantum detection in bioelectrode multi-electrode recordings of human iPSC-derived neurons and axonal networks (R-11434), i-BOF; EU Quanteria II Project Maestro; EU Horizon 2020 project Amadeus grant agreements ID: 101080136 and No. 101046911 QuMicro. M.G. acknowledges the Eu project No. 101038045 (ChemIQS): This Project has received funding from the European Union's Horizon 2020 research and innovation programme. The work was also supported by the Czech Science Foundation projects no. 23-04876S and No. 20-28980s, the European Regional Development Funds, OP RDE, Project: CARAT (No. CZ.02.1.01/0.0/0.0/16_026/0008382), and by the Czech Academy of Sciences - Strategy AV21 - Research Program VP29. The irradiation of HPHT nanodiamonds by electrons was supported through the Czech Academy of Sciences Project No. RVO61389005. The authors also acknowledge the support from FWO (Funds for Scientific Research Flanders), projects No. G0D1721N and No. G0A0520N. Grand Challenge i-BOF UHasselt project: 'Nanoscale diamond probes to modulate temperature-sensitive ion channels in neurons and phagocyte' and GACR project No: 20-28980s. The authors are grateful to David Chvatil for the electron irradiation of HPHT nanodiamonds. Correction added on December 11, 2023, after first online publication: The author byline was corrected.

Conflict of Interest

The authors declare no conflict of interest.

Data Availability Statement

The data that support the findings of this study are available in the supplementary material of this article.

Keywords

chemical vapor deposition, fluorescent nanodiamonds, nitrogen-vacancy (NV) spin relaxometry, quantum sensing

Received: January 11, 2023

Revised: July 17, 2023

Published online: October 13, 2023

- [1] Y. Wu, T. Weil, *Adv. Sci.* **2022**, 9, 2200059.
- [2] T. Zhang, G. Pramanik, K. Zhang, M. Gulka, L. Wang, J. Jing, F. Xu, Z. Li, Q. Wei, P. Cigler, Z. Chu, *ACS Sens.* **2021**, 6, 2077.
- [3] A. Mzyk, Y. Ong, A. R. Ortiz Moreno, S. K. Padamati, Y. Zhang, C. A. Reyes-San-Martin, R. Schirhagl, *Anal. Chem.* **2022**, 94, 225.
- [4] A. Jarmola, V. M. Acosta, K. Jensen, S. Chemerisov, D. Budker, *Phys. Rev. Lett.* **2012**, 108, 197601.
- [5] L. Rondin, J.-P. Tetienne, T. Hingant, J.-F. Roch, P. Maletinsky, V. Jacques, *Rep. Prog. Phys.* **2014**, 77, 056503.
- [6] C. L. Degen, M. Poggio, H. J. Mamin, D. Rugar, *Phys. Rev. Lett.* **2007**, 99, 250601.
- [7] T. Staudacher, F. Shi, S. Pezzagna, J. Meijer, J. Du, C. A. Meriles, F. Reinhard, J. Wrachtrup, *Science* **2013**, 339, 561.
- [8] D. R. Glenn, D. B. Bucher, J. Lee, M. D. Lukin, H. Park, R. L. Walsworth, *Nature* **2018**, 555, 351.
- [9] J.-X. Qin, X.-G. Yang, C.-F. Lv, Y.-Z. Li, K.-K. Liu, J.-H. Zang, X. Yang, L. Dong, C.-X. Shan, *Mater. Des.* **2021**, 210, 110091.
- [10] A. Ermakova, G. Pramanik, J.-M. Cai, G. Algara-Siller, U. Kaiser, T. Weil, Y.-K. Tzeng, H. C. Chang, L. P. McGuinness, M. B. Plenio, B. Naydenov, F. Jelezko, *Nano Lett.* **2013**, 13, 3305.

- [11] J.-P. Boudou, P. A. Curmi, F. Jelezko, J. Wrachtrup, P. Aubert, M. Sennour, G. Balasubramanian, R. Reuter, A. Thorel, E. Gaffet, *Nanotechnology* **2009**, *20*, 235602.
- [12] J. Barton, M. Gulka, J. Tarabek, Y. Mindarava, Z. Wang, J. Schimer, H. Raabova, J. Bednar, M. B. Plenio, F. Jelezko, M. Nesladek, P. Cigler, *ACS Nano* **2020**, *14*, 12938.
- [13] T. de Guillebon, B. Vindolet, J.-F. Roch, V. Jacques, L. Rondin, *Phys. Rev. B* **2020**, *102*, 16.
- [14] R. Schirhagl, K. Chang, M. Loretz, C. L. Degen, *Annu. Rev. Phys. Chem.* **2014**, *65*, 83.
- [15] P. Reineck, L. F. Trindade, J. Havlik, J. Stursa, A. Heffernan, A. Elbourne, A. Orth, M. Capelli, P. Cigler, D. A. Simpson, B. C. Gibson, *Part. Part. Syst. Charact.* **2019**, *36*, 1900009.
- [16] J. Havlik, V. Petrakova, J. Kucka, H. Raabova, D. Panek, V. Stepan, Z. Zlamalova Cilova, P. Reineck, J. Stursa, J. Kucera, M. Hruby, P. Cigler, *Nat. Commun.* **2018**, *9*, 4467.
- [17] H. S. Knowles, D. M. Kara, M. Atatüre, *Nat. Mater.* **2014**, *13*, 21.
- [18] B. D. Wood, G. A. Stimpson, J. E. March, Y. N. D. Lekhai, C. J. Stephen, B. L. Green, A. C. Frangeskou, L. Ginés, S. Mandal, O. A. Williams, G. W. Morley, *Phys. Rev. B* **2022**, *105*, 205401.
- [19] M. E. Trusheim, L. Li, A. Laraoui, E. H. Chen, H. Bakhrü, T. Schröder, O. Gaathon, C. A. Meriles, D. Englund, *Nano Lett.* **2014**, *14*, 32.
- [20] S. Mandal, *RSC Adv.* **2021**, *11*, 10159.
- [21] M. A. Gebbie, H. Ishiwata, P. J. McQuade, V. Petrak, A. Taylor, C. Freiwald, J. E. Dahl, R. M. K. Carlson, A. A. Fokin, P. R. Schreiner, Z.-X. Shen, M. Nesladek, N. A. Melosh, *Proc. Nat. Acad. Sci.* **2018**, *115*, 8284.
- [22] Y.-K. Tzeng, J. L. Zhang, H. Lu, H. Ishiwata, J. Dahl, R. M. K. Carlson, H. Yan, P. R. Schreiner, J. Vučković, Z.-X. Shen, N. Melosh, S. Chu, *Nano Lett.* **2017**, *17*, 1489.
- [23] A. Fokin, P. Schreiner, N. Fokina, B. Tkachenko, H. Hausmann, M. Serafin, J. Dahl, S. Liu, R. Carlson, *J. Org. Chem.* **2006**, *71*, 8532.
- [24] H. Ishiwata, *Molecular Diamonds Enabled Synthesis and Growth*, Stanford University, Stanford, CA **2015**.
- [25] M. Nesladek, D. Tromson, P. Bergonzo, P. Hubik, J. Mares, J. Kristofik, D. Kindl, O. Williams, D. Gruen, *Diamond Relat. Mater.* **2006**, *15*, 607.
- [26] G. Balasubramanian, P. Neumann, D. Twitchen, M. Markham, R. Kolesov, N. Mizuochi, J. Isoya, J. Achard, J. Beck, J. Tessler, V. Jacques, P. Hemmer, F. Jelezko, *Nat. Mater.* **2009**, *8*, 383.
- [27] G. Degutis, P. Pobodinskas, S. Turner, Y.-G. Lu, S. Al Riyami, B. Ruttens, T. Yoshitake, J. D'Haen, K. Haenen, J. Verbeeck, A. Hardy, M. Van Bael, *Diamond Relat. Mater.* **2016**, *64*, 163.
- [28] P. Soille, L. M. Vincent, in *Visual Communications and Image Processing '90: Fifth in a Series*, (Ed.: M. Kunt), vol. 1360, International Society for Optics and Photonics, SPIE, Bellingham, Washington **1990**, pp. 240–250.
- [29] M. Daenen, L. Zhang, R. Erni, O. A. Williams, A. Hardy, M. K. Van Bael, P. Wagner, K. Haenen, M. Nesládek, G. Van Tendeloo, *Adv. Mater.* **2009**, *21*, 670.
- [30] A. Tallaire, M. Lesik, V. Jacques, S. Pezzagna, V. Mille, O. Brinza, J. Meijer, B. Abel, J. Roch, A. Gicquel, J. Achard, *Diamond Relat. Mater.* **2015**, *51*, 55.
- [31] A. M. Edmonds, U. F. S. D'Haenens-Johansson, R. J. Cruddace, M. E. Newton, K.-M. C. Fu, C. Santori, R. G. Beausoleil, D. J. Twitchen, M. L. Markham, *Phys. Rev. B* **2012**, *86*, 035201.
- [32] J. A. van Wyk, E. C. Reynhardt, G. L. High, I. Kiflawi, *J. Phys. D: Appl. Phys.* **1997**, *30*, 1790.
- [33] C. Wild, R. Kohl, N. Herres, W. Müller-Sebert, P. Koidl, *Diamond Relat. Mater.* **1994**, *3*, 373.
- [34] G. Knuyt, M. Nesládek, C. Quaeys, L. Stals, *Diamond Relat. Mater.* **1998**, *7*, 1095.
- [35] I. C. Barbosa, J. Gutsche, A. Widera, *Phys. Rev. B* **2023**, *108*, 07541.
- [36] V. Petrakova, A. Taylor, I. Kratochvilová, F. Fendrych, J. Vacik, J. Kucka, J. Štursa, P. Cigler, M. Ledvina, A. Fiserova, P. Kneppo, M. Nesladek, *Adv. Funct. Mater.* **2012**, *22*, 812.
- [37] Z. Zhang, J. T. Yates, *Chem. Rev.* **2012**, *112*, 5520.
- [38] M. Tachiki, T. Fukuda, K. Sugata, H. Seo, H. Umezawa, H. Kawarada, *Appl. Surf. Sci.* **2000**, *159-160*, 578.
- [39] B. A. Myers, A. Ariyaratne, A. C. B. Jayich, *Phys. Rev. Lett.* **2017**, *118*, 197201.
- [40] D. Bluvstein, Z. Zhang, A. C. B. Jayich, *Phys. Rev. Lett.* **2019**, *122*, 076101.
- [41] D. Wirtitsch, G. Wachter, S. Reisenbauer, M. Gulka, V. Ivády, F. Jelezko, A. Gali, M. Nesladek, M. Trupke, *Phys. Rev. Res.* **2023**, *5*, 013014.
- [42] J. Stursa, J. Havlik, V. Petrakova, M. Gulka, J. Ralis, V. Zach, Z. Pulec, V. Stepan, S. A. Zargaleh, M. Ledvina, M. Nesladek, F. Treussart, P. Cigler, *Carbon* **2016**, *96*, 812.
- [43] L. P. McGuinness, Y. Yan, A. Stacey, D. A. Simpson, L. T. Hall, D. Maclaurin, S. Praver, P. Mulvaney, J. Wrachtrup, F. Caruso, R. E. Scholten, L. C. L. Hollenberg, *Nat. Nanotechnol.* **2011**, *6*, 358.
- [44] A. Taylor, F. Fendrych, L. Fekete, J. Vlček, V. Řezáčová, V. Petrák, J. Krucký, M. Nesládek, M. Liehr, *Diamond Relat. Mater.* **2011**, *20*, 613.
- [45] Z. Vlčková Živcová, V. Mortet, A. Taylor, A. Zukal, O. Frank, L. Kavan, *Diamond Relat. Mater.* **2018**, *87*, 61.
- [46] E. Bourgeois, A. Jarmola, M. Gulka, J. Hruby, D. Budker, M. Nesladek, *Nat. Commun.* **2015**, *6*, 8577.
- [47] A. Jarmola, A. Berzins, J. Smits, K. Smits, J. Prikulis, F. Gahbauer, R. Ferber, D. Erts, M. Auzinsh, D. Budker, *Appl. Phys. Lett.* **2015**, *107*, 242403.